Modeling joints with clearance and friction in multibody dynamic simulation of automotive differentials

Geoffrey Virlez,[a] Olivier Brüls, Emmanuel Tromme, and Pierre Duysinx
Department of Aerospace and Mechanical Engineering (LTAS), University of Liège, Liège 4000, Belgium

(Received 25 September 2012; accepted 30 October 2012; published online 10 January 2013)

Abstract Defects in kinematic joints can sometimes highly influence the simulation response of the whole multibody system within which these joints are included. For instance, the clearance, the friction, the lubrication and the flexibility affect the transient behaviour, reduce the component life and produce noise and vibration for classical joints such as prismatics, cylindrics or universal joints. In this work, a new 3D cylindrical joint model which accounts for the clearance, the misalignment and the friction is presented. This formulation has been used to represent the link between the planet gears and the planet carrier in an automotive differential model. [doi:10.1063/2.1301303]

Keywords cylindrical joint, clearance, friction, automotive differential, multibody dynamics

Kinematic joints are key components in multibody simulation tools. Most of the time, the joints are represented with idealized models which restrain the motion of the entire system by a set of kinematic constraints. This kind of formulation often considers the joints as perfect rigid elements without any default but has the advantages to be simple to implement and are computationally efficient. However, physical phenomena such as clearance, misalignment, flexibility, friction, lubrication or impact can highly influence the dynamic response of the joints and have a non negligible effect on the accuracy and reliability of the full multibody model. For instance, the modelling of the joints between the suspension arm and the car body with bushing elements strongly influences the vehicle dynamic simulation.[1]

The representation of the bodies submitted to the kinematic joints with their actual geometry and their material flexibility properties is without doubt the most accurate way to model any kind of joints. Contact conditions defined between finite element models of the bodies subjected to spherical joints are used in Ref. 1. Such detailed models are able to capture a lot of disruptive factors but they are often quite complex to achieve and they highly increase the computational time.

Other models of joints are at an intermediate level of complexity between the two aforementioned categories. These global joint representations enable to account for some disrupting effects without increasing much the number of degree of freedom. In Ref. 2, the influence of clearance and lubrication is studied for the hinge and spherical joints within the framework of energy preserving and decaying time integration schemes. A planar revolute joint model with clearance based on a continuous contact model is described in Ref. 3. The nonsmooth dynamic approach can also be used to represent kinematic joints with defects, see for example.[4,5] This approach often allows to use larger time steps but needs specific integration methods such as time-stepping or event-driven schemes.

The objective of this work is to develop a global model for a cylindrical joint where the clearance, the misalignment and friction force are accounted for. A continuous force law is used to model the contact between the pin and the internal cylinder which are represented as rigid bodies. The joint described in this paper has been tested in a full TORSEN differential multibody model.

This new joint model has been implemented within the framework of the nonlinear finite element method for multibody systems described in Ref. 6. This approach enables the modelling of complex mechanical systems composed of rigid and flexible bodies, kinematics joints and force elements. The configuration is represented using absolute nodal coordinates with respect to a unique inertial frame. Hence, there is no distinction between rigid and elastic coordinates which allows accounting in a natural way for many nonlinear flexible effects and large deformations.

The dynamics of a system including holonomic bilateral constraints is described by

$$\boldsymbol{M}(\boldsymbol{q})\ \ddot{\boldsymbol{q}} + \boldsymbol{g}(\boldsymbol{q},\dot{\boldsymbol{q}},t) + \boldsymbol{\Phi}_{\boldsymbol{q}}^{\mathrm{T}}(p\boldsymbol{\Phi} + k\boldsymbol{\lambda}) = \boldsymbol{0}, \tag{1}$$

$$k\ \boldsymbol{\Phi}(\boldsymbol{q},t) = \boldsymbol{0}, \tag{2}$$

where $\boldsymbol{q}$, $\dot{\boldsymbol{q}}$ and $\ddot{\boldsymbol{q}}$ are the generalized displacements, velocities and acceleration coordinates, $\boldsymbol{M}(\boldsymbol{q})$ is the mass matrix, $\boldsymbol{g}(\boldsymbol{q},\dot{\boldsymbol{q}},t) = \boldsymbol{g}^{\mathrm{gyr}}(\boldsymbol{q},\dot{\boldsymbol{q}}) + \boldsymbol{g}^{\mathrm{int}}(\boldsymbol{q},\dot{\boldsymbol{q}}) - \boldsymbol{g}^{\mathrm{ext}}(t)$, with $\boldsymbol{g}^{\mathrm{gyr}}$ the vector of the complementary inertia forces, $\boldsymbol{g}^{\mathrm{int}}(\boldsymbol{q},\dot{\boldsymbol{q}})$ the vector of the internal forces, e.g., elastic and dissipations forces, and $\boldsymbol{g}^{\mathrm{ext}}(t)$ the vector of the external forces. According to the augmented Lagrangian method, the constraint forces are formulated by $\boldsymbol{\Phi}_{\boldsymbol{q}}^{\mathrm{T}}(p\boldsymbol{\Phi} + k\boldsymbol{\lambda})$, where $\boldsymbol{\lambda}$ is the vector of Lagrange multipliers related to the algebraic bilateral constraints ($\boldsymbol{\Phi} = \boldsymbol{0}$); k and p are respectively a scaling and a penalty factor to improve the numerical conditioning.

Equations (1) and (2) form a system of nonlinear differential-algebraic equations. The solution is evaluated step by step using a second order accurate time

[a] Corresponding author. Email: Geoffrey.Virlez@ulg.ac.be.

integration scheme. For this study, the Chung–Hulbert scheme, which belongs to the family of the generalized α-method, has been used (see Refs. 7 and 8). At each time step, a system of nonlinear algebraic equations has to be solved using a Newton–Raphson method.

The cartesian rotation vector combined with an updated Lagrangian approach is used for the parametrization of rotations. This choice enables an exact representation of large rotations. The tangent operator $\boldsymbol{T}(\boldsymbol{\Psi}_{\text{inc}})$ allows computing the material variation of rotations $\delta\boldsymbol{\Theta}$ from the variation of the incremental cartesian rotation vector $\delta\boldsymbol{\Psi}_{\text{inc}}$ as

$$\delta\boldsymbol{\Theta} = \boldsymbol{T}(\boldsymbol{\Psi}_{\text{inc}})\ \delta\boldsymbol{\Psi}_{\text{inc}}. \tag{3}$$

In a cylindrical joint, according to the kind of mechanism considered the contact between the pin and the external surface of the hollow cylinder can occur at one point, at two points or on a line. In this work, in order to simplify the joint formulation, it is assumed that the contact takes place only at the top or at the bottom of the pin. The contact element developed in this work models the interactions between the cylindrical face of the hollow cylinder and one extremity of the pin. Therefore, the joint needs to be used twice for each pin: One time for each extremity.

The direction of the contact and friction forces depends on the geometry of the pin and the inner cylinder near the contact point and can be hardly determined in case of intricate configurations: sharped edge or small fillet radius on the pin external surface for example. The objective of this study is not to analyse detailed phenomena at the contact location but to have a global representation of the related dynamic phenomena. Therefore, in order to have a simple formulation for this 3D contact element, the top and the bottom of the cylinder are considered as having a spherical shape (see Fig. 1). This assumption seems reasonable in practical situations where the clearance is small and the relative inclination of the pin is limited since the contact point would then remain close to the intersection circle between the sphere and the cylinder. It would thus be close to the physical contact point even if the geometry of the cylinder edge is not precisely represented.

This new joint is defined by two physical nodes attached on the two rigid bodies candidate to contact. The node A is located on the axis of the hollow cylinder and the node B is fixed at the center of the top or bottom circular face of the pin which is also the center of the contact sphere. The positions and velocities of the twelve absolute nodal coordinates are involved in the expression of this contact element.

A material local frame attached to each body is used in the joint formulation. The triads of orthogonal unit vectors $\{\boldsymbol{e}''_{A_1}, \boldsymbol{e}''_{A_2}, \boldsymbol{e}''_{A_3}\}$ and $\{\boldsymbol{e}''_{B_1}, \boldsymbol{e}''_{B_2}, \boldsymbol{e}''_{B_3}\}$ have their origin fixed respectively at the point A of the hollow cylinder and at the point B of the pin. The first triad vectors $\boldsymbol{e}''_{A_1}$ and $\boldsymbol{e}''_{B_1}$ are aligned with the axis of the cylinders. The second triad vectors $\boldsymbol{e}''_{A_2}, \boldsymbol{e}''_{B_2}$ are arbitrary oriented in the plane perpendicular to $\boldsymbol{e}''_{A_1}$ and

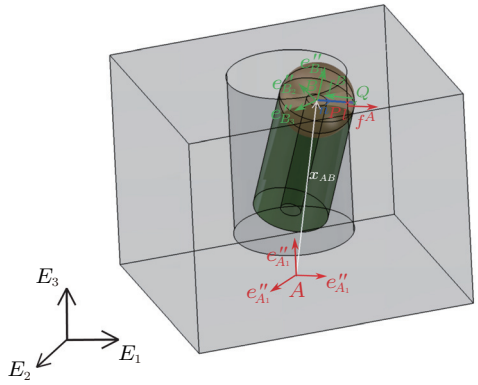

Fig. 1. Contact force.

$\boldsymbol{e}''_{B_1}$. The third unit vectors $\boldsymbol{e}''_{A_3}$, $\boldsymbol{e}''_{B_3}$ complete the dextrorsum reference frame.

The vectors $\boldsymbol{e}_{A_i}$, $\boldsymbol{e}_{B_i}$ represent the orientation of the two material frames at the initial configuration. In this work, for simplicity the pin and the hollow cylinder are positioned with parallel axis at the initial time. Consequently, the initial orientation is equivalent for the two material frames

$$\boldsymbol{e}_{A_i} = \boldsymbol{R}_1\ \boldsymbol{E}_i = \boldsymbol{e}_{B_i}, \tag{4}$$

where $\boldsymbol{R}_1$ is the rotation matrix giving the initial orientation of the material frames with respect to the absolute inertial frame $\{\boldsymbol{E}_1, \boldsymbol{E}_2, \boldsymbol{E}_3\}$.

The rotation operators $\boldsymbol{R}_A$, $\boldsymbol{R}_B$ give the orientation of bodies A and B from the initial to the current configuration

$$\boldsymbol{e}''_{A_i} = \boldsymbol{R}_A\ \boldsymbol{e}_{A_i} = \boldsymbol{R}_A\ \boldsymbol{R}_1\ \boldsymbol{E}_i, \tag{5}$$
$$\boldsymbol{e}''_{B_i} = \boldsymbol{R}_B\ \boldsymbol{e}_{B_i} = \boldsymbol{R}_B\ \boldsymbol{R}_1\ \boldsymbol{E}_i. \tag{6}$$

The points P and Q in Fig. 1 are the approximated contact points respectively on the rigid bodies A and B due to the geometrical assumptions introduced previously. The position vectors $\boldsymbol{x}_P, \boldsymbol{x}_Q$ of these contact points can be easily computed according to the positions $\boldsymbol{x}_A, \boldsymbol{x}_B$ of the nodes A and B, the rotation matrices $\boldsymbol{R}_A, \boldsymbol{R}_1$ and the radii r_A, r_B of the contact surfaces near the contact points (see Eqs. (17) and (18)).

The contact force is defined by the continuous impact model theory developed in Ref. 9. This penalty method is based on the Hertz law and uses the penetration (l) as a representation of the local deformation of the two bodies in contact. In addition to the stiffness term, this contact model (Eq. (7)) also includes a hysteresis damping term which enables to represent the kinetic energy loss during the impact process. This loss of kinetic energy is described by a restitution coefficient and depends on the shapes and material properties of the colliding bodies as well as their relative velocities. The restitution coefficient e has a value comprised between 0 (plastic contact) and 1 (no energy loss) and can be seen as the absolute value of the ratio of the relative velocity after and before the impact. In order to avoid a

jump at the beginning of the contact and tension force at the end, the classical viscous damping term ($c\dot{l}$) has been multiplied by l^n.

The impact-contact force law is expressed as

$$f_c(l,\dot{l}) = \begin{cases} kl^n + cl^n\dot{l}, & \text{if} \quad l > 0 \\ 0, & \text{if} \quad l \leqslant 0 \end{cases} \tag{7}$$

with the exponent n equal to 1.5 for circular and elliptic contact areas. The case when the penetration length l has a negative value means that the contact is not effective and consequently no contact force has to be applied.

In case of global multibody models, the contact stiffness parameter k is often determined by analytical formulations. For a sphere in contact with an internal cylinder, a few approximate expressions are available in Ref. 10 for a good approximation of the contact stiffness k.

One way to set the damping parameter c consists in formulating this coefficient as a function of the restitution coefficient. According to the contact configuration, various expressions can be found in Ref. 11. The formulation proposed in Ref. 12 has been chosen for the definition of the damping parameter c

$$c = \frac{8\,(1-e)}{5\;e}\frac{k}{\dot{l}_s}, \tag{8}$$

where $\dot{l}_s$ is the relative normal velocity between bodies at the time of contact establishment. This expression has the advantage to can be used whatever the amount of energy dissipation while most definitions of the damping parameter c are only valid for high values of the restitution coefficient ($e > 0.8$).

The continuous contact force model does not involve any kinematic constraint. Therefore the contribution of this force element to the motion equations (Eq. (1)) of the multibody system is only contained in the term of internal forces, $\boldsymbol{g}^{\text{int}}(\boldsymbol{q},\dot{\boldsymbol{q}})$. The virtual work principle is used in order to formulate the internal force vector of this contact element

$$\delta W_n = \delta\boldsymbol{x}_P^{\mathrm{T}}\;\boldsymbol{f}^A + \delta\boldsymbol{x}_Q^{\mathrm{T}}\;\boldsymbol{f}^B, \tag{9}$$

where $\boldsymbol{x}_P$, $\boldsymbol{x}_Q$ are the position vectors expressed in the absolute frame of the contact point P on the body A and of the contact point Q on the body B (see Fig. 1), and $\boldsymbol{f}^A$, $\boldsymbol{f}^B$ are the contact forces respectively applied on bodies A and B.

In order to express the virtual displacements $\delta\boldsymbol{x}_P$ and $\delta\boldsymbol{x}_Q$, the points P and Q are considered rigidly fixed on bodies A and B

$$\delta\boldsymbol{x}_P = \delta\boldsymbol{x}_A + \delta\boldsymbol{\theta}_A \times \boldsymbol{x}_{AP}, \tag{10}$$
$$\delta\boldsymbol{x}_Q = \delta\boldsymbol{x}_B + \delta\boldsymbol{\theta}_B \times \boldsymbol{x}_{BQ}, \tag{11}$$

with $\boldsymbol{x}_{ij} = \boldsymbol{x}_j - \boldsymbol{x}_i$.

The relation between the variation of the spatial angular vector $\delta\boldsymbol{\theta}$ and the material angular variation vector $\delta\boldsymbol{\Theta}$ is provided by the initial rotation matrix $\boldsymbol{R}_1$ and the rotation operators $\boldsymbol{R}_A$, $\boldsymbol{R}_B$ as

$$\delta\boldsymbol{\theta}_A = \boldsymbol{R}_1\boldsymbol{R}_A\;\delta\boldsymbol{\Theta}_A, \tag{12}$$
$$\delta\boldsymbol{\theta}_B = \boldsymbol{R}_1\boldsymbol{R}_B\;\delta\boldsymbol{\Theta}_B. \tag{13}$$

In this work, the skew-symmetric matrix $\widetilde{\boldsymbol{i}}$ formed with the components of the vector $\boldsymbol{i}$ is often used to replace the cross products by matrix products ($\boldsymbol{i}\times\boldsymbol{j} = \widetilde{\boldsymbol{i}}\;\boldsymbol{j}$). The virtual displacement of P and Q can be reformulated as

$$\delta\boldsymbol{x}_P = \delta\boldsymbol{x}_A - \widetilde{\boldsymbol{x}}_{AP}\boldsymbol{R}_1\boldsymbol{R}_A\;\delta\boldsymbol{\Theta}_A, \tag{14}$$
$$\delta\boldsymbol{x}_Q = \delta\boldsymbol{x}_B - \widetilde{\boldsymbol{x}}_{BQ}\boldsymbol{R}_1\boldsymbol{R}_B\;\delta\boldsymbol{\Theta}_B. \tag{15}$$

The unit vector $\boldsymbol{n}$ normal to the collision surface between the sphere and the hollow cylinder and aligned with the vector $\boldsymbol{x}_{PQ}$ of maximal indentation l can be defined as

$$\boldsymbol{n} = \frac{\left(\boldsymbol{I} - \boldsymbol{e}''_{A_1}\boldsymbol{e}''^{\,\mathrm{T}}_{A_1}\right)\boldsymbol{x}_{AB}}{\left\|\left(\boldsymbol{I} - \boldsymbol{e}''_{A_1}\boldsymbol{e}''^{\,\mathrm{T}}_{A_1}\right)\boldsymbol{x}_{AB}\right\|}, \tag{16}$$

where $\boldsymbol{e}''_{A_1}$ is the first axis of the material local frame attached to the node A (see Eq. 5).

The vector $\boldsymbol{x}_{AP}$ and $\boldsymbol{x}_{BQ}$ can be expressed according to the normal vector $\boldsymbol{n}$ and the distance vector $\boldsymbol{x}_{AB}$ as

$$\boldsymbol{x}_{BQ} = r_B\;\boldsymbol{n}, \tag{17}$$
$$\boldsymbol{x}_{AP} = \boldsymbol{x}_{AB} + \boldsymbol{x}_{BQ} + \boldsymbol{x}_{QP} = \boldsymbol{x}_{AB} + (r_B - l)\;\boldsymbol{n}, \tag{18}$$

with r_B the radius of the sphere attached at the top of the pin.

The contact forces $\boldsymbol{f}_A$ and $\boldsymbol{f}_B$ are aligned with the normal direction $\boldsymbol{n}$ and their magnitude f_c is given by the contact law (Eq. (7))

$$\boldsymbol{f} = \boldsymbol{f}^B = -\boldsymbol{f}^A = f_c\;\boldsymbol{n}. \tag{19}$$

f_c depends on the relative normal deformation l and deformation velocity $\dot{l}$, which are computed according to the following expressions

$$l = \boldsymbol{x}_{PQ}^{\mathrm{T}}\;\boldsymbol{n} = \boldsymbol{x}_{AB}^{\mathrm{T}}\;\boldsymbol{n} + r_B - r_A, \tag{20}$$
$$\dot{l} = \dot{\boldsymbol{x}}_{PQ}^{\mathrm{T}}\;\boldsymbol{n} + \boldsymbol{x}_{PQ}^{\mathrm{T}}\;\dot{\boldsymbol{n}}, \tag{21}$$

where the second term of $\dot{l}$ is always null because $\boldsymbol{x}_{PQ}$ is parallel to $\boldsymbol{n}$ whereas $\dot{\boldsymbol{n}}$ is perpendicular to $\boldsymbol{n}$. The vector $\dot{\boldsymbol{x}}_{PQ}$ can be obtained owing to the difference of velocity vector of P and Q

$$\dot{\boldsymbol{x}}_P = \dot{\boldsymbol{x}}_A + \boldsymbol{\omega}_A \times \boldsymbol{x}_{AP}, \tag{22}$$
$$\dot{\boldsymbol{x}}_Q = \dot{\boldsymbol{x}}_B + \boldsymbol{\omega}_B \times \boldsymbol{x}_{BQ}. \tag{23}$$

The spatial angular velocity vector $\boldsymbol{\omega}$ can be transformed to the material angular velocity vector $\boldsymbol{\Omega}$ by

$$\boldsymbol{\omega}_A = \boldsymbol{R}_1\boldsymbol{R}_A\;\boldsymbol{\Omega}_A, \tag{24}$$
$$\boldsymbol{\omega}_B = \boldsymbol{R}_1\boldsymbol{R}_B\;\boldsymbol{\Omega}_B. \tag{25}$$

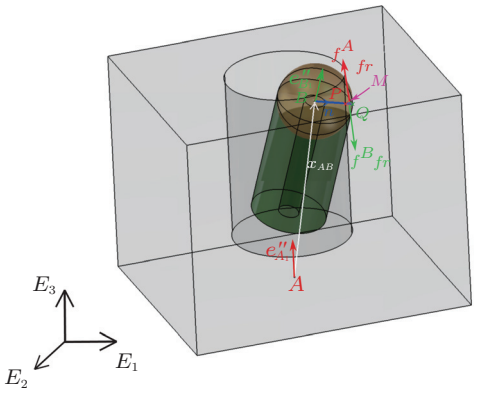

Fig. 2. Friction force.

Finally, the virtual work expression (Eq. (9)) can be reformulated as

$$\delta W_n = \Big(\delta \boldsymbol{x}_{AB}^{\mathrm{T}} + \delta \boldsymbol{\Theta}_B^{\mathrm{T}} \boldsymbol{R}_B^{\mathrm{T}} \boldsymbol{R}_1^{\mathrm{T}}\, \widetilde{\boldsymbol{x}}_{BQ} - \delta \boldsymbol{\Theta}_A^{\mathrm{T}} \boldsymbol{R}_A^{\mathrm{T}} \boldsymbol{R}_1^{\mathrm{T}}\, \widetilde{\boldsymbol{x}}_{AP}\Big) \boldsymbol{f}. \tag{26}$$

The internal force vector $\boldsymbol{g}_n^{\mathrm{int}}$ (Eq. (29)) of this normal contact force can be easily obtained by identification of the last expression with the classical virtual work expression for a force element

$$\delta W = \delta \boldsymbol{q}^{\mathrm{T}}\ \boldsymbol{g}^{\mathrm{int}}\,(\boldsymbol{q}, \dot{\boldsymbol{q}})\,, \tag{27}$$

where $\boldsymbol{q}$ is the vector of generalized coordinates involved in the force element. For the contact model developed here, the vector $\boldsymbol{q}$ includes the absolute nodal degree of freedom in translation and rotation of the nodes A and B.

$$\boldsymbol{q} = \begin{Bmatrix} \boldsymbol{x}_A \\ \boldsymbol{\Psi}_{A\mathrm{inc}} \\ \boldsymbol{x}_B \\ \boldsymbol{\Psi}_{B\mathrm{inc}} \end{Bmatrix}, \tag{28}$$

$$\boldsymbol{g}_n^{\mathrm{int}}(\boldsymbol{q}, \dot{\boldsymbol{q}}) = f_{\mathrm{c}} \begin{Bmatrix} -\boldsymbol{n} \\ -\boldsymbol{T}^{\mathrm{T}}(\boldsymbol{\Psi}_{A\mathrm{inc}}) \boldsymbol{R}_A^{\mathrm{T}} \boldsymbol{R}_1^{\mathrm{T}} \widetilde{\boldsymbol{x}}_{AB}\ \boldsymbol{n} \\ \boldsymbol{n} \\ \boldsymbol{0} \end{Bmatrix}. \tag{29}$$

The friction forces $\boldsymbol{f}_{\mathrm{fr}}^A$ and $\boldsymbol{f}_{\mathrm{fr}}^B$ encountered at the contact between the bodies A and B are considered applied on the point M, located at the middle between the points P and Q (Fig. 2).

The virtual work of the friction forces can be expressed as

$$\delta W_{\mathrm{fr}} = \delta \boldsymbol{x}_M^{A^{\mathrm{T}}}\ \boldsymbol{f}_{\mathrm{fr}}^A + \delta \boldsymbol{x}_M^{B^{\mathrm{T}}}\ \boldsymbol{f}_{\mathrm{fr}}^B, \tag{30}$$

where $\delta \boldsymbol{x}_M^A$ is the virtual displacement when M is considered attached to the body A, and $\delta \boldsymbol{x}_M^B$ is the virtual displacement when M is considered attached to the body B. By analogy with Eqs. (14) and (15), the

1: Housing 4: Intermal gear
2: Sun gear 5: Coupling
3: Planet gears 6: Case
7, 8, 9, 10, 11: Thrust washers

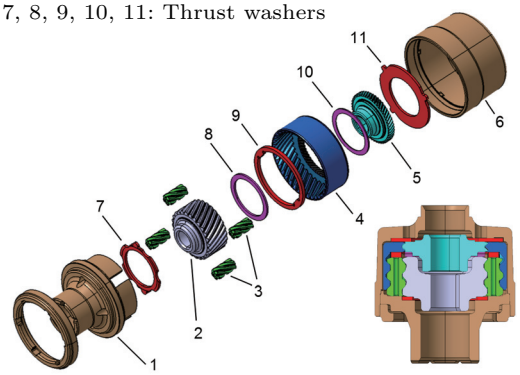

Fig. 3. Kinematic diagram, exploded view and cut-away view of type C TORSEN differential.

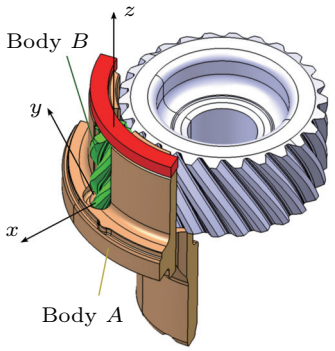

Fig. 4. Test model for the new joint in the geometrical configuration of TORSEN differential.

expression of these virtual displacements can be easily obtained as

$$\delta \boldsymbol{x}_M^A = \delta \boldsymbol{x}_A - \widetilde{\boldsymbol{x}}_{AM} \boldsymbol{R}_1 \boldsymbol{R}_A \delta \boldsymbol{\Theta}_A, \tag{31}$$

$$\delta \boldsymbol{x}_M^B = \delta \boldsymbol{x}_B - \widetilde{\boldsymbol{x}}_{BM} \boldsymbol{R}_1 \boldsymbol{R}_B \delta \boldsymbol{\Theta}_B. \tag{32}$$

The vectors $\boldsymbol{x}_{AM}$ and $\boldsymbol{x}_{BM}$ between the nodes A and B and the application point M of the friction force can be formulated according to $\boldsymbol{x}_{AB}$, $\boldsymbol{n}$, r_B and l as

$$\boldsymbol{x}_{AM} = \boldsymbol{x}_{AP} + \frac{l}{2}\boldsymbol{n} = \boldsymbol{x}_{AB} + \left(r_B - \frac{l}{2}\right)\boldsymbol{n}, \tag{33}$$

$$\boldsymbol{x}_{BM} = \boldsymbol{x}_{BQ} - \frac{l}{2}\boldsymbol{n} = \left(r_B - \frac{l}{2}\right)\boldsymbol{n}. \tag{34}$$

The friction forces are aligned with the normal vector $\boldsymbol{n}$ but have opposite directions ($\boldsymbol{f}_{\mathrm{fr}} = \boldsymbol{f}_{\mathrm{fr}}^B = -\boldsymbol{f}_{\mathrm{fr}}^A$) and are defined by

$$\boldsymbol{f}_{\mathrm{fr}} = -\mu_{\mathrm{R}}(v_t)\ f_{\mathrm{c}}\ \boldsymbol{t}, \tag{35}$$

where f_{c} is the magnitude of the normal contact force (see Eq. (7)), $\boldsymbol{t}$ is the unit tangential vector described hereafter, and μ_{R} is the regularized friction coefficient which allows to avoid the large discontinuity when the sign of the relative sliding velocity shifts.

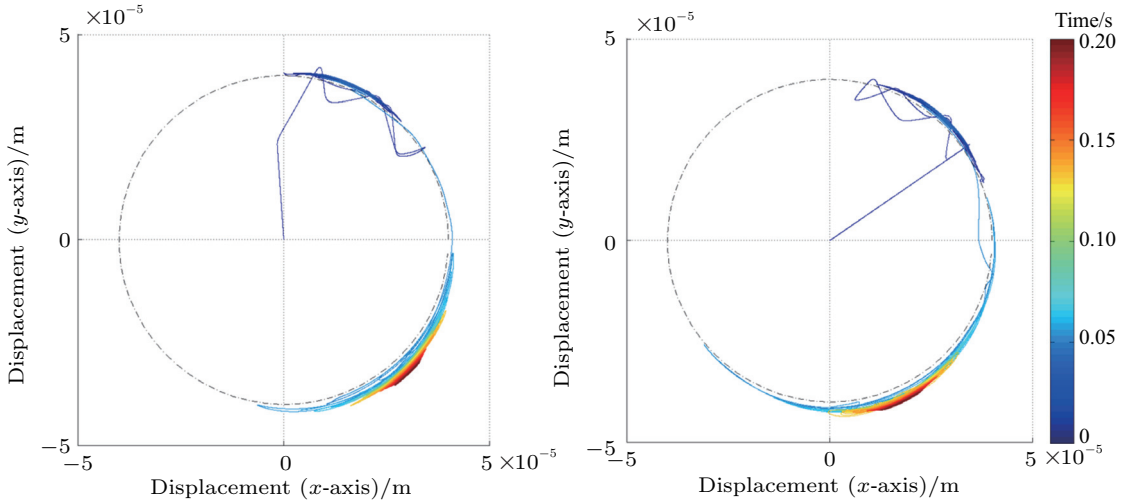

(a) Bottom face center (b) Top face center

Fig. 5. Trajectory of the face center relative to the center of the housing cavity.

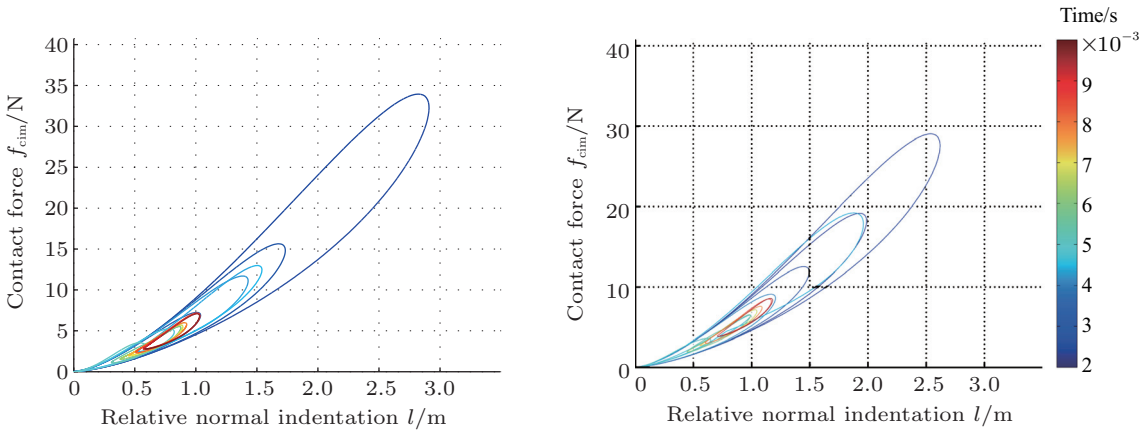

(a) Planet gear bottom (b) Planet gear top

Fig. 6. Hysteresis loops of the contact force illustrating the energy dissipation for the first impacts.

The unit tangential vector $\boldsymbol{t}$ can be simply expressed by $\boldsymbol{t} = \boldsymbol{v}_t / v_t$ where $\boldsymbol{v}_t$ is the vector of tangential velocity at the point M where the friction forces are applied, and is expressed as

$$\boldsymbol{v}_t = \left(\boldsymbol{I} - \boldsymbol{n}\boldsymbol{n}^{\mathrm{T}}\right)\left(\dot{\boldsymbol{x}}_M^B - \dot{\boldsymbol{x}}_M^A\right), \tag{36}$$

in which $\dot{\boldsymbol{x}}_M^A$ and $\dot{\boldsymbol{x}}_M^B$ are the velocity vectors when the point M is respectively attached to the bodies A and B.

$$\dot{\boldsymbol{x}}_M^A = \dot{\boldsymbol{x}}_A + \boldsymbol{\omega}_A \times \boldsymbol{x}_{AM}, \tag{37}$$
$$\dot{\boldsymbol{x}}_M^B = \dot{\boldsymbol{x}}_B + \boldsymbol{\omega}_B \times \boldsymbol{x}_{BM}. \tag{38}$$

The virtual work expression of the friction forces can be reformulated as

$$\delta W_{\text{fr}} = \Big(\delta \boldsymbol{x}_{AB}^{\mathrm{T}} + \delta \boldsymbol{\Theta}_B^{\mathrm{T}} \boldsymbol{R}_B^{\mathrm{T}} \boldsymbol{R}_1^{\mathrm{T}}\ \widetilde{\boldsymbol{x}}_{BM} - \delta \boldsymbol{\Theta}_A^{\mathrm{T}} \boldsymbol{R}_A^{\mathrm{T}} \boldsymbol{R}_1^{\mathrm{T}}\ \widetilde{\boldsymbol{x}}_{AM}\Big) \boldsymbol{f}_{\text{fr}}. \tag{39}$$

The identification with Eq. (27) is straightforward and allows to obtain the vector of internal forces $\boldsymbol{g}_{\text{fr}}^{\text{int}}$

$$\boldsymbol{g}_{\text{fr}}^{\text{int}}(\boldsymbol{q}, \dot{\boldsymbol{q}}) = \begin{Bmatrix} -\boldsymbol{f}_{\text{fr}} \\ -\boldsymbol{T}^{\mathrm{T}}(\boldsymbol{\Psi}_{A\text{inc}}) \boldsymbol{R}_A^{\mathrm{T}} \boldsymbol{R}_1^{\mathrm{T}} \widetilde{\boldsymbol{x}}_{AM}\ \boldsymbol{f}_{\text{fr}} \\ \boldsymbol{f}_{\text{fr}} \\ \boldsymbol{T}^{\mathrm{T}}(\boldsymbol{\Psi}_{B\text{inc}}) \boldsymbol{R}_B^{\mathrm{T}} \boldsymbol{R}_1^{\mathrm{T}} \widetilde{\boldsymbol{x}}_{BM}\ \boldsymbol{f}_{\text{fr}} \end{Bmatrix}. \tag{40}$$

The tangent stiffness and damping matrices have been computed analytically but are not given in this paper for the sake of conciseness.

The new joint presented hereabove has been tested to model the link between the planet gears and the planet carrier in a type C TORSEN differential. As depicted in Fig. 3, this central differential is mainly composed of a epicyclic gear, several thrust washers and a housing in two parts. The friction encountered by the contact between the planet gears and the housing as well as between the gear wheels and the thrust washers

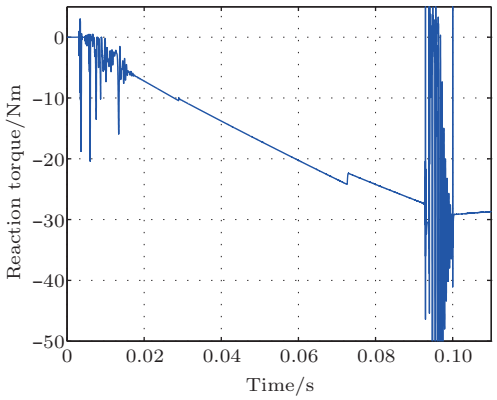

Fig. 7. Transient variations of resistant torque on coupling due to clearance and misalignment at the beginning of the simulation.

is at the origin of the locking effect and torque transfer of TORSEN differentials.

The assembly of planet gears on planet carrier is particular in this mechanical device. Indeed, planet gears are inserted in housing cylindrical cavities without any physical rotational axis. The clearance between crater and planet gear diameters allows planet gears to tilt which involves contact between gear teeth top and crater external surface. The friction occurred by these contacts tends to slow down the relative rotation and significantly contributes to the locking effect. The transient behaviour at the switching time between two working modes is also highly influenced by this specific assembly.

In addition to the 4 planet gear/housing joints, the global model also includes 15 rigid bodies, 8 gear pairs, 14 contact elements, and 1 screw joint. The number of generalized coordinates is about 800.

In order to study in a simple way, the behavior of the new cylindrical joint in the configuration of the TORSEN differential, only a reduced part of the differential has been modeled in a first instance. As depicted in Fig. 4, this simple system includes the sun gear, a unique planet gear, the housing and one thrust washer. The housing and the thrust washer are clamped to the ground. The sun gear is linked to the housing with a hinge joint and is submitted to a torque linearly increasing from 0 Nm at $t = 0$ s to 10 Nm for the period $t = [0.02,\ 0.04]$ s and before decreasing, following a linear function to -20 Nm for the period $t = [0.06,\ 0.2]$ s. The planet gear is meshing with the sun gear; its displacement in the x–y plane is constrained by the new joint developed in this work; its axial displacement in the z-axis is constrained by two unilateral contact conditions (one defined with the housing and one defined with the thrust washer).

The displacement in the x–y plane of the top and bottom face center of the planet gear inside the housing hole is depicted in Fig. 5. At the initial time, the planet gear is located at the center of the housing cavity and their axis are parallel. As soon as a torque is applied on the sun gear, the meshing force tends to increase the distance between gear wheels rotation axis and the planet gear is deported against the circular face of housing cavity. After the first impact, the planet gear undergoes several rebonds and afterwards tends to keep a constant global orientation until the torque applied on the gear wheel changes of sign. At this time, the planet gear quickly moves to negative values of y-axis and also tend to maintain a fixed position after the transient period. Due to the helical gear teeth, the planet gear is tilted during the transient phases, which explains the small differences of trajectory observed on Fig. 5(a) compared with Fig. 5(b).

Figure 6 illustrates for the first impacts the kinetic energy dissipation which is taken into account by the contact law (Eq. (7)). Indeed, the hysteresis loops encircle the amount of energy dissipated owing to the damping term used in the contact force. The areas of these hysteresis loops highly depends on the choice of the restitution coefficient. In this example, this coefficient has been fixed to 0.8, a frequently used value for contacts between two metallic bodies.

Finally, the new cylindrical joint formulation has been introduced in a full TORSEN differential model. For this simulation the same configuration as experimental settings on testrig has been reproduced. A torque is progressively applied on one output shaft whereas the rotation velocity is prescribed on the second output and the housing is clamped on the test bench. Figure 7 depicts the resistant torque which allows to limit the rotation velocity of the sun gear when a 50 Nm torque is applied in 0.1 s on the coupling. The spikes at the beginning of the simulation ($t = [0,\ 0.02]$ s) are caused by the shocks due to the clearance in the cylindrical joints. The discontinuities observed during the second part of the simulation are due to the contact establishment between the gear wheels and the thrust washers. For instance, the friction inherent to the contact between the internal gear and the thrust washer #11 modifies the friction torques in the differential as soon as this unilateral contact is active and explains the step on the curve at $t = [0.07,\ 0.08]$ s. Although the transient behavior is influenced by the imperfections of the joints, the mean value of the resistant torque is similar to the value obtained if the PG/housing joints are modeled with idealized cylindrics.

In conclusion, the non-ideal cylindrical joint presented in this paper accounts for several imperfections often encountered in mechanical joints: clearance, misalignment, friction and impact forces. The formulation is based on a continuous impact force law to model the contacts between the pin tips and the lateral face of the hollow cylinder. The loss of kinetic energy at each impact is accounted for by a restitution coefficient introduced inside the damping parameter. This new joint has been tested within a TORSEN differential multibody model in order to represent the assembly of the planet gears on the planet carrier. However, for this kind of complex industrial system which includes numerous discontinuous and nonlinear phenomena and where the ef-

forts transmitted are high, the continuous contact models require very small time steps ($h \leqslant 10^{-6}$ s) to insure the convergence of the integration algorithm. The modelling of contacts with nonsmooth techniques may be an alternative to avoid this drawback and permit faster simulation of global multibody systems with non-ideal kinematic joints (see preliminary work in Ref. 13).

The author Geoffrey Virlez would like to acknowledge the Belgian National Fund for Scientific research (FRIA) for its financial support.

1. J. Ambróosio, and P. Versissimo, Multibody System Dynamics **22**, 341 (2009).
2. O. Bauchau, and J. Rodriguez, International Journal of Solids and Structures **39**, 41 (2002).
3. P. Flores, Nonlinear Dynamics **61**, 633 (2010).
4. P. Flores, L. Remco, and C. Glocker, Multibody System Dynamics **23**, 165 (2009).
5. Y. Dumont, and L. Paoli, International Journal of Computer Applications in Technology **33**, 41 (2008).
6. M. Géradin and A. Cardona, *Flexible Multibody Dynamics: A Finite Element Approach* (John Wiley & Sons, New York, 2001).
7. J. Chung, and G. Hulbert, ASME Journal of Applied Mechanics **60**, 371 (1993).
8. M. Arnold, and O. Brüls, Multibody System Dynamics **18**, 185 (2007).
9. H. Lankarani, Canonical equations of motion and estimation of parameters in the analysis of impact problems, [Ph.D. Thesis], University of Arizona, USA (1988).
10. M. J. Puttock, and E. G. Thwaite, *Elastic Compression of Spheres and Cylinders at Point and Line Contact*, Research Report 25 (Commonwealth Scientific and Industrial Research Organization, Australia, 1969).
11. H. Lankarani, and P. Nikravesh, Nonlinear Dynamics **5**, 193 (1994).
12. P. Flores, M. Machado, and M. T. Silva, et al., Multibody System Dynamics **25**, 357 (2011).
13. Q. Z. Chen, V. Acary, and G. Virlez, et al., in: *Proceedings of the Second Joint International Conference on Multibody System Dynamics*, Germany (2012).